Journal of Colloid and Interface Science 673 (2024) 788–796

Contents lists available at ScienceDirect

Journal of Colloid And Interface Science

journal homepage: www.elsevier.com/locate/jcis

Regular Article

# Ring-shaped colloidal patterns on saline water films

Michiel A. Hack [a], Marjolein N. van der Linden [b,a], Herman Wijshoff [b,c,1], Jacco H. Snoeijer [a], Tim Segers [d,*]

[a] Physics of Fluids Group, Max Planck Center Twente for Complex Fluid Dynamics, Faculty of Science and Technology, University of Twente, P.O. Box 217, Enschede, 7500 AE, the Netherlands
[b] Canon Production Printing Netherlands B.V., P.O. Box 101, Venlo, 5900 MA, the Netherlands
[c] Department of Mechanical Engineering, Eindhoven University of Technology, P.O. Box 513, Eindhoven, 5600 MB, the Netherlands
[d] BIOS/Lab on a Chip Group, Max Planck Center Twente for Complex Fluid Dynamics, MESA+ Institute for Nanotechnology, Faculty of Electrical Engineering, Mathematics and Computer Science, University of Twente, P.O. Box 217, Enschede, 7500 AE, the Netherlands

## GRAPHICAL ABSTRACT

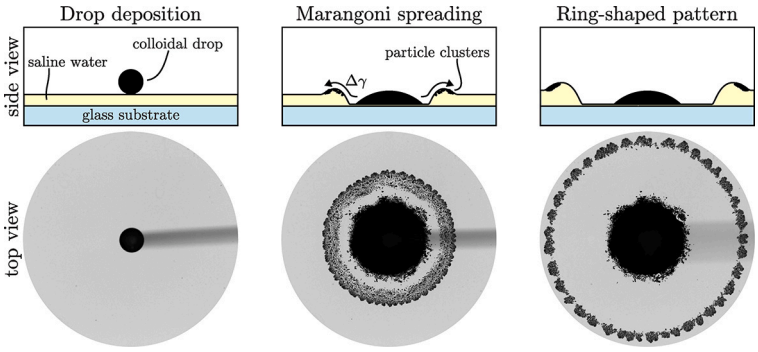


## ARTICLE INFO

*Keywords:*
Colloids
Pattern formation
Drops
Spreading
Thin films
Marangoni flow

## ABSTRACT

*Hypothesis:* Electrostatically stabilised colloidal particles destabilise when brought into contact with cations causing the particles to aggregate in clusters. When a drop with stabilised colloidal partices is deposited on a liquid film containing cations the delicate balance between the fluid-mechanical and physicochemical properties of the system governs the spreading dynamics and formation of colloidal particle clusters.
*Experiments:* High-speed imaging and digital holographic microscopy were used to characterise the spreading process.
*Findings:* We reveal that a spreading colloidal drop evolves into a ring-shaped pattern after it is deposited on a thin saline water film. Clustered colloidal particles aggregate into larger trapezoidally-shaped 'supraclusters'. Using a simple model we show that the trapezoidal shape of the supraclusters is determined by the transition from inertial spreading dynamics to Marangoni flow. These results may be of interest to applications such as *wet-on-wet* inkjet printing, where particle destabilisation and hydrodynamic flow coexist.

* Corresponding author.
*E-mail address:* t.j.segers@utwente.nl (T. Segers).
[1] Herman passed away on May 10, 2023. He was key to the conceptualisation of this research and made valuable contributions to the interpretation of the results. He will be sadly missed.

https://doi.org/10.1016/j.jcis.2024.06.015
Received 14 January 2024; Received in revised form 1 June 2024; Accepted 3 June 2024
Available online 10 June 2024

## 1. Introduction

The deposition and subsequent spreading of a drop on a substrate is a crucial process in numerous technological applications, such as lithography [1] and inkjet printing [2–4]. Many technologies rely on multicomponent liquids and involve liquid substrates. Ink, for example, typically consists of water, pigment, and several other components that control the liquid properties of the ink [5], and is sometimes deposited on another (still wet) layer of ink in a technique called *wet-on-wet* printing [6]. Spreading in such systems is fundamentally different from a single-component drop spreading on a solid substrate [7,8]. For example, the equilibrium contact angle of a multicomponent drop may be unexpectedly large due to physicochemical processes that occur inside (and around) the drop [9,10]. Likewise, the spreading of drops on liquid substrates can introduce a plethora of intriguing phenomena depending on the system properties, ranging from new dynamics [11,12] to fingering instabilities [13] and pattern formation [14,15].

In wet-on-wet inkjet printing a salty substrate coating called a *primer layer* is used to overcome the conflicting requirements of ink during the various stages of the inkjet printing process [3,6,16,17]. Clustering of pigment (i.e., colloidal particles) is undesirable during and prior to the jetting phase because large clusters can clog the inkjet nozzle [2] or lead to jetting failure due to bubble nucleation and entrainment [18]. Conversely, rapid clustering of pigment ('solidification' [4]) *is* desirable during the impact and drying phase because large clusters are unable to follow the liquid flow into to the porous (paper) substrate [19] and into neighbouring inks with different colours [3], thereby ensuring bright colours and sharp lines, respectively [16,17].

In the present work, we investigate the spreading of a colloidal drop on a thin saline water film. This system closely resembles the spreading of an ink drop on a primer layer. The colloidal particles used in our experiment are electrostatically stabilised by negatively charged molecular groups attached to the particles. Upon contact between the drop and the film, cations in the saline water film destabilise the colloidal suspension by lowering the energy barrier present between the particles [20,21] such that the colloidal particles aggregate into clusters [5]. We reveal that this physicochemical destabilisation mechanism, in combination with the hydrodynamic flow encountered in drop spreading on liquid substrates, results in intricate ring-shaped patterns. An example of such a pattern is presented in Fig. 1, which show the deposition of a millimetre-sized colloidal drop on a micrometres-thick saline water film. Fig. 1 shows that the drop initially spreads uniformly in all directions. Soon after contact, however, the contact line develops an undulating shape and clusters of colloidal particles become visible. These clusters subsequently separate from the drop and aggregate in larger trapezoidally-shaped 'supraclusters' (see the inset of Fig. 1) that form the ring-shaped pattern. In the context of wet-on-wet printing, the combination of particle destabilisation and hydrodynamic flow can thus lead to undesired particle deposition phenomena, as evidenced by Fig. 1. This work investigates, for the first time, the interaction between the simultaneous processes of colloidal destabilisation and hydrodynamic flow with the aim to understand the ring-shaped pattern formation dynamics observed in Fig. 1.

## 2. Methods

### 2.1. Experimental procedure

The experiment consists of depositing a colloidal drop (volume $V = 5$ µL) on a thin saline water film and observing the subsequent pattern formation. Two high-speed cameras were used to simultaneously record the dynamics from the top (Nova S12 camera, Photron with LM50TC lens, Kowa) and side view (Nova S12 camera, Photron with 12× zoom lens, Navitar) perspectives at 10 000 frames per second. The top view perspective was used to observe the pattern formation process, while the side view perspective was used to accurately determine the moment of first (visible) contact between the drop and the film's surface (which we define as $t = 0$), and to measure the initial spreading dynamics of the drop. Two light sources were used to illuminate the experiment from the side (KL2500, Schott) and below

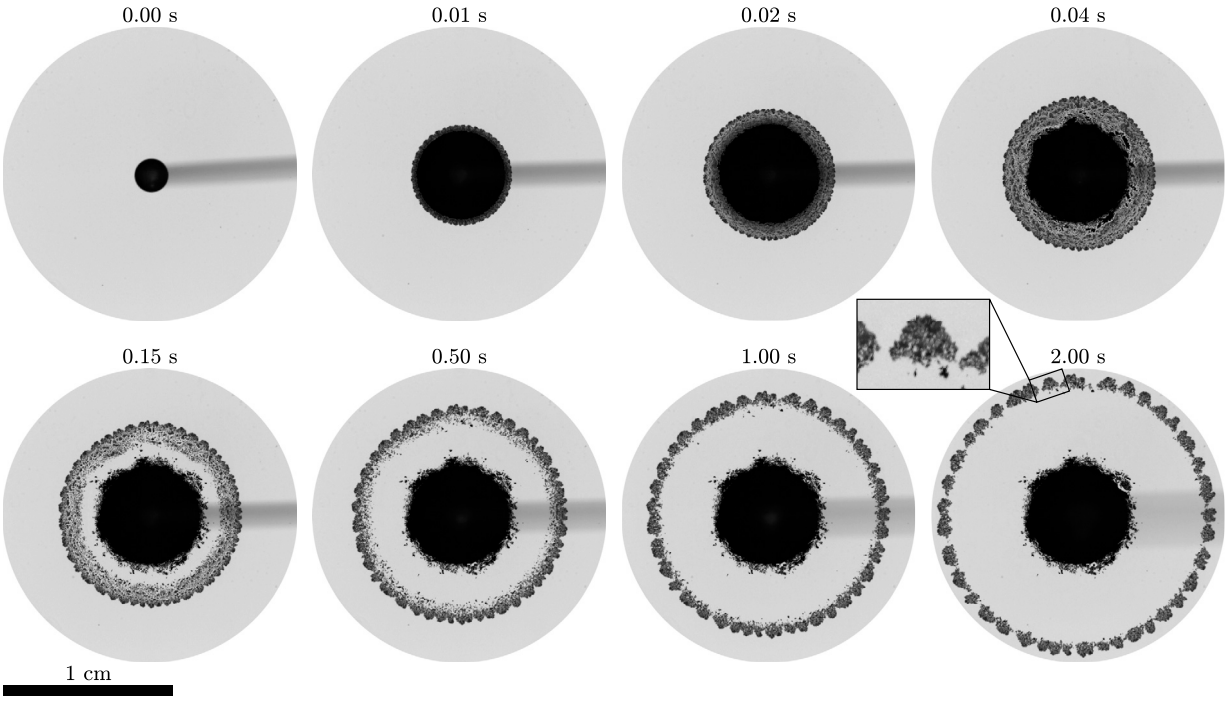


**Fig. 1.** Image sequence (top view) showing the deposition of a colloidal drop ($c_d = 10$ wt%) on a $c_f = 30$ wt% saline water film with $h_0 \approx 20$ µm, and subsequent pattern formation. The dark circle with ragged edge that remains in the centre of the ring is the drop. The dark unfocused horizontal line extending from the centre to the edge of the image is the needle used to deposit the drop. The inset shows a close-up image of one of the supraclusters showing their characteristic trapezoidal shape. See the Supplementary Material for the corresponding movie (Movie S1).

(uniform LED backlight, Phlox). A different bottom lighting technique with a divergent light source (KL2500, Schott) was used for several experiments to reveal the curvature of the liquid-air interface of the saline water film. The drops were generated on a needle (26 gauge, Hamilton Company) by a syringe pump (PHD2000, Harvard Apparatus). To ensure reproducible and gentle deposition of the drops, the needle was moved towards the surface of the thin film by a programmable linear motor (T-LSR150B, Zaber) with a velocity ($\approx 0.01$ m/s, calibrated) that was much smaller than the typical contact line velocity during the initial spreading phase ($\approx 0.42$ m/s, based on the example side-view images in Fig. 8a). The experiments were performed at room temperature ($\approx 20 \pm 1\,^{\circ}$C, Super EX Sensor, TFA) and in ambient conditions (relative humidity $\approx 40 \pm 3\%$, Super EX Sensor, TFA) because the evaporation of the drop and film are negligible (discussed in Secs. 2.3 and 2.4). A schematic drawing of the experimental setup is shown in Fig. S1 in Sec. S1 of the Supplementary Material.

### 2.2. Digital holographic microscopy

In a separate experiment, the locations of the clusters with respect to deformations of the surface of the thin saline water films were measured using digital holographic microscopy (abbreviated DHM, model T-1000, Lyncée Tec with 2.5× lens) [22,23]. This technique allows real-time simultaneous measurement of both the surface morphology of the liquid film and the location of the clusters by reconstructing both phase and intensity images from holograms at 12.5 frames per second (Koala reconstruction software, Lyncée Tec). An example of raw measurement data is shown in Fig. S2 in Sec. S2 of the Supplementary Material.

### 2.3. Colloidal suspensions

The colloidal particles used were carbon black pigment particles (CAB-O-JET 400, CABOT Corporation). These particles (with a diameter of approximately 130 nm) are functionalised with geminal bisphosphonic acid groups that stabilise the suspension by means of electrostatic repulsions between the particles [24,25]. The mass concentration $c_d$ of the colloids in the suspension was controlled through dilution of the stock suspension ($c_{d,stock} = 15$ wt%) with highly-purified water (MilliQ, Millipore Corporation). The surface tensions of the suspensions were measured using the pendent drop method. They were found to be independent of the particle concentration and always equal to that of pure water, see Fig. S3 in Sec. S3 of the Supplementary Material. The time scale associated with the evaporation of sessile drops is typically of the order of several minutes, whereas Fig. 1 shows that the patterns typically form in a matter of seconds, we thus expect that the evaporation of the drop is insignificant [26,27].

### 2.4. Thin saline water films

The salt solutions were prepared by dissolving calcium chloride ($CaCl_2$, Sigma-Aldrich) in water. The solutions were vigorously shaken until they were uniformly transparent, and were allowed to cool down to room temperature before use. $CaCl_2$ dissociates into calcium cations ($Ca^{2+}$, which is responsible for the destabilisation of the colloidal particles upon contact with the drop) and chloride anions ($Cl^-$) when dissolved in water. Glass microscope slides (76×26 mm, Menzel-Gläser) were used as base substrates for the thin saline water films. These were cleaned with acetone and water, blow-dried with nitrogen, and finally treated with plasma (PDC-002, Harrick Plasma) to induce hydrophilicity such that a stable film can be prepared. Note that the wettability of the substrates does not influence the experiments since the range of molecular interactions is well below the range of film thicknesses used in the experiments. Uniform films were obtained by spin-coating the glass substrates with the $CaCl_2$-solutions. The film thickness $h_0$ was controlled through the spinning time of the spin-coater, and was measured prior to use for each film using reflectometry (HR2000+ spectrometer with HL-2000-FHSA halogen light source, Ocean Optics). We measured the thickness of each film at five different locations to confirm uniformity of the film. The thickness range over which we performed measurements ($h_0 \approx 3$ to 24 μm) was determined by the ability to obtain uniform films using this method. The refractive index (used for the thickness measurements) and viscosity were taken from literature [28,29]. The surface tension of the $CaCl_2$-solutions increases approximately linear with the $CaCl_2$ mass concentration $c_f$ (due to their ionic nature) to approximately 87 mN/m at $c_f = 40$ wt%, see Fig. S3 in Sec. S3 of the Supplementary Material. We did not perform measurements beyond $c_f = 40$ wt% to stay well below the solubility limit of $CaCl_2$. The densities of the $CaCl_2$-solutions, which were used to determine the surface tension, were measured using a densimeter (DMA 35, Anton Paar). We have verified that the film thickness (and thus the composition of the liquid) remains approximately constant over time and that it is not strongly affected by evaporation of the liquid; see Sec. S4 in the Supplementary Material.

## 3. Phenomenology of the pattern formation process

We first provide a qualitative overview of the phenomenology of the pattern formation process. The formation of a pattern for typical parameters ($c_d = 10$ wt%, $c_f = 30$ wt%, and $h_0 \approx 20$ μm) is presented in Fig. 1. When the colloidal drop is deposited on the saline water film (at $t = 0$) it starts spreading with a high radial velocity ($\approx 0.6$ m/s during the initial times of measurement). During this outward inertial drop spreading motion, the contact line develops an undulate shape (visible at $t = 0.01$ s). Simultaneously, colloidal particles form clusters due to their destabilisation by the presence of $Ca^{2+}$ cations in the film. These clusters are first observed in Fig. 1 at $t = 0.02$ s. Remarkably, some clusters separate from the drop (the dark central zone) after it has reached its final equilibrium shape (at $t = 0.04$ s), resulting in the emergence of a ring-shaped collection of particle clusters ($t \geq 0.15$ s). The radius of the ring increases over time, though at a velocity that is smaller than the initial spreading velocity of the drop (note the different timescales in Fig. 1). Furthermore, the clusters at the outermost edge of the ring move at a lower radial velocity than the clusters at the innermost edge of the ring. As a result, the clusters in the ring merge such that the width of the ring decreases over time (cf., the ring width at $t = 0.15$ s and $t = 2.00$ s). As its radius continues to grow, the ring eventually breaks up into trapezoidally-shaped 'supraclusters' (at $t = 2.00$ s). This breakup occurs when all clusters have merged with the bulk of the ring,

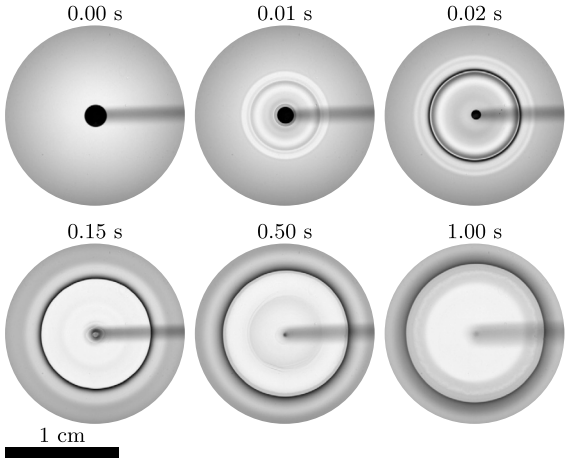


**Fig. 2.** Image sequence (top view) showing the deposition of a water drop (without particles, $c_d = 0$) on a $c_f = 30$ wt% saline water film with $h_0 \approx 20$ μm. A surface tension gradient is generated by the difference between the surface tension of the drop and the film, which leads to the formation of a circular thin region in the film and an outward moving Marangoni rim.

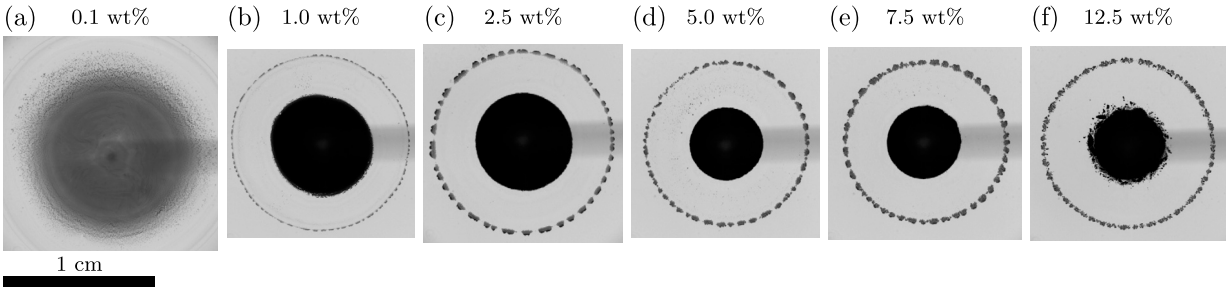


**Fig. 3.** Effect of the mass concentration of colloids $c_d$. Patterns observed for (a) $c_d = 0.1$ wt%, (b) $c_d = 1.0$ wt%, (c) $c_d = 2.5$ wt%, (d) $c_d = 5.0$ wt%, (e) $c_d = 7.5$ wt%, and (f) $c_d = 12.5$ wt%. For all cases $t = 1.00$ s, $c_f = 30$ wt%, and $h_0 \approx 9$ μm. The scale bar applies to all images to allow direct comparison of the images. The ring-shaped pattern only appears for sufficiently high $c_d$.

and the number of supraclusters is set by the wavelength of the undulate shape of the contact line. Finally, at large times ($t \geq 2.00$ s in Fig. 1), the (now separated) supraclusters continue their radially outward translation and their morphology does not change anymore.

The results presented thus far suggest that the appearance of the ring-shaped pattern is a consequence of the simultaneous destabilisation of colloidal particles and spreading of the drop. In the following, we therefore systematically investigate the effect of the properties of the colloidal drop ($c_d$) and the thin saline water film ($c_f$ and $h_0$) on the phenomenology of the pattern.

### 3.1. Effect of the colloidal concentration $c_d$

We first consider the effect of the colloidal particles in the drop. Fig. 2 shows an experiment under the same conditions as the experiment shown in Fig. 1, but now without any colloidal particles in the drop (i.e., $c_d = 0$). The illumination technique with a divergent backlight (instead of the uniform LED backlight) was used for this experiment, which allows changes in the curvature of the saline water film's surface to be visualised as changes in the image intensity. The dynamics of the rim in Fig. 2 are remarkably similar to that of the (supra)cluster ring in Fig. 1. An important difference, however, is that the undulate shape of the contact line (which determines the final number of supraclusters in the ring) is not present when $c_d = 0$. This means that the undulate shape of the contact line is not caused by purely hydrodynamic mechanisms such as the Saffman-Taylor instability or surface tension-driven fingering [13,30]. Instead, it is the presence of the colloidal particles that causes the undulating contact line morphology.

Fig. 3 shows several patterns obtained for various $c_d > 0$ at $t = 1.00$ s with $c_f = 30$ wt% and $h_0 \approx 9$ μm. The ring-shaped pattern appears only for sufficiently large $c_d$. While small clusters are visible for $c_d = 0.1$ wt% (Fig. 3a), they do not aggregate in a clear ring. On the contrary, the pattern is present for all $c_d \geq 1.0$ wt% (Fig. 3b–f), though small differences can be observed. For example, the supracluster size increases with $c_d$ up to $c_d \approx 7.5$ wt% and then decreases with $c_d$, as shown in Fig. 4a. Finally, we observe that the size of the clusters prior to aggregating in the ring increases with $c_d$, resulting in visible gaps in the supraclusters (see, e.g., Fig. 3f; close-up images are available in Fig. S7 in Sec. S6 in the Supplementary Material).

### 3.2. Effect of the salt concentration $c_f$

In addition to $c_d$, the $CaCl_2$ concentration $c_f$ also plays an important role in the formation of the ring-shaped pattern. The influence of $c_f$ is twofold: it affects both the destabilisation of particles and the hydrodynamics of the saline water film—its surface tension $\gamma$ (see Fig. S3 in Sec. S3 of the Supplementary Material) and viscosity $\eta$ both increase with $c_f$ [29]. Fig. 5 shows several patterns obtained for various $c_f$ at $t = 1.00$ s with $c_d = 10$ wt% and $h_0 \approx 9$ μm. When $c_f = 0$ (i.e., when the substrate is pure water, see Fig. 5a), we observe neither an undulation of the contact line nor a ring-shaped pattern. Instead, the drop spreads out uniformly, without the visible formation of particle clusters at any point during the spreading process since there are no cations present that destabilise the colloidal particles.

In Fig. 5b–f, we show patterns obtained for various $c_f > 0$. The ring-shaped pattern appears only for sufficiently large $c_f$. Notably, even a small amount of $CaCl_2$ has a strong effect on the morphology of the contact line—a deformation of the contact line (though non-periodic) can be observed for concentrations as low as $c_f = 0.01$ wt% (Fig. 5b). This is strong evidence that particle destabilisation plays a critical role for the pattern formation, since the difference in surface tension and viscosity between these $c_f$ is small, yet the contact line behaves completely differently.

No significant effect is observed by further increasing $c_f$ (Fig. 5c) until $c_f \geq 5$ wt% (Fig. 5d), for which clusters that separate from the centre drop are first observed. This is accompanied by a qualitative change in the spreading behaviour: the drop reaches an equilibrium contact angle $\theta > 0$ for $c_f \geq 5$ wt%, whereas $\theta = 0$ for $c_f < 5$ wt%, see Fig. S9 in Sec. S7 of the Supplementary Material. However, while clusters do separate from the drop at $c_f = 5$ wt%, the pattern is notably different from the patterns observed for higher $c_f$—the seperated clusters do not move radially outward for a significant amount of time and do not form a clear ring-shaped pattern. A further increase of $c_f$ beyond $c_f = 5$ wt% (Fig. 5e–f) does not significantly change the qualitative features of the pattern. In both cases a ring-shaped pattern emerges due to the formation and radially outward motion of clusters. The supracluster size, however, does show a dependence on $c_f$ in this range, with the maximum supracluster size obtained when $c_f = 20$ wt%, see Fig. 4a.

### 3.3. Effect of the film thickness $h_0$

Finally, we turn to the film thickness $h_0$ of the saline water film. Fig. 6 shows a series of experiments in which we varied $h_0$ with $c_d = 10$ wt% and $c_f = 30$ wt% fixed. The ring-shaped pattern appears

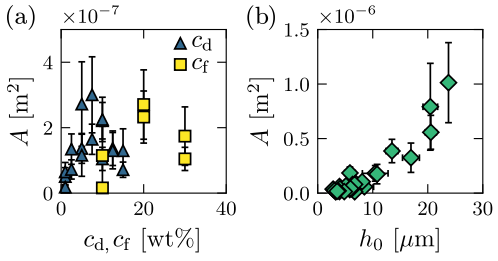


**Fig. 4.** Supracluster size (expressed as area $A$) as a function of (a) the mass concentration of colloids $c_d$ and the mass concentration of $CaCl_2$ $c_f$, and (b) the film thickness $h_0$. The base system is $c_d = 10$ wt%, $c_f = 30$ wt%, $h_0 \approx 9$ μm, with one of the parameters being systematically varied. In (b) the horizontal error bar indicates the standard deviation of five thickness measurements at five different locations on the film. The method used to determine $A$ is discussed in Sec. S5 in the Supplementary Material (as well as the vertical error bar).

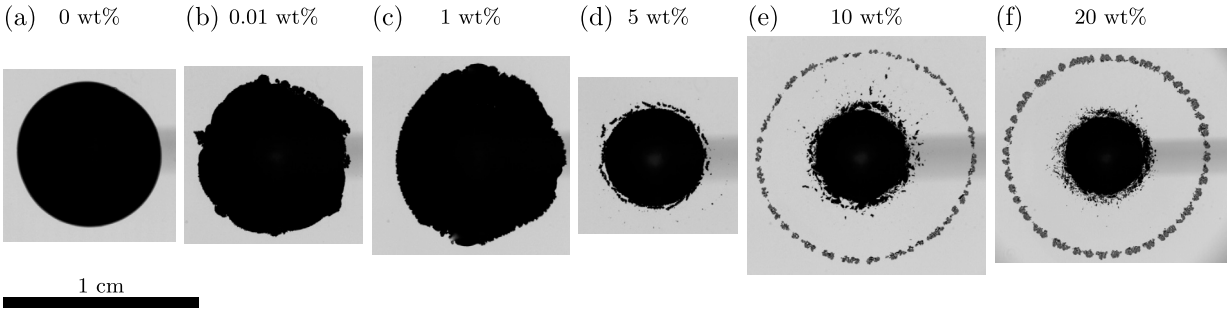


**Fig. 5.** Effect of the mass concentration of $CaCl_2$ $c_f$. Patterns observed for (a) $c_f = 0$ wt%, (b) $c_f = 0.01$ wt%, (c) $c_f = 1$ wt%, (d) $c_f = 5$ wt%, (e) $c_f = 10$ wt%, and (f) $c_f = 20$ wt%. For all cases $t = 1.00$ s, $c_d = 10$ wt%, and $h_0 \approx 9$ μm. The scale bar applies to all images to allow direct comparison of the images. The ring-shaped pattern only appears for sufficiently high $c_f$.

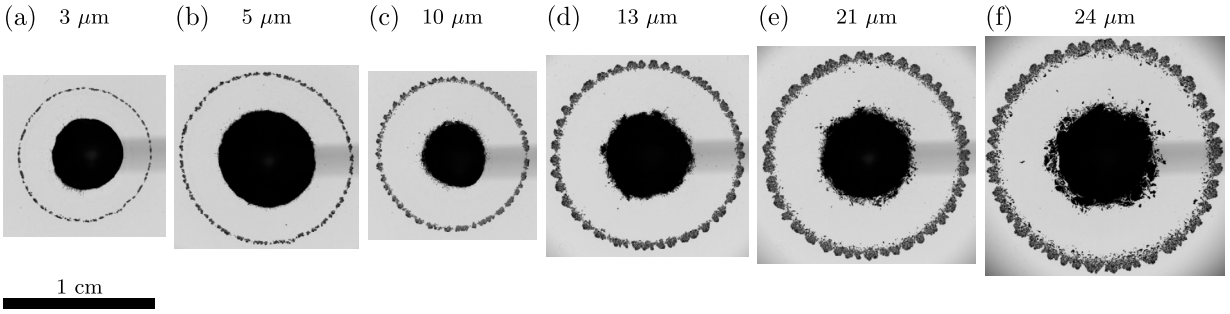


**Fig. 6.** Effect of the film thickness $h_0$. Patterns observed for (a) $h_0 \approx 3$ μm, (b) $h_0 \approx 5$ μm, (c) $h_0 \approx 10$ μm, (d) $h_0 \approx 13$ μm, (e) $h_0 \approx 21$ μm, and (f) $h_0 \approx 24$ μm. For all cases $t = 1.00$ s, $c_d = 10$ wt%, and $c_f = 30$ wt%. The scale bar applies to all images to allow direct comparison of the images. The width of the ring shows a strong dependence on $h_0$.

for all $h_0$ in Fig. 6, although two features of the pattern show a strong dependence on $h_0$. First, the radius of the ring (shown at $t = 1.00$ s in Fig. 6) increases with $h_0$. The glass substrate imposes a no-slip boundary condition, such that the average flow velocity in the saline water film is higher for larger $h_0$. As a result, the ring radius is larger for thicker films than it is for thinner films, as is indeed observed in Fig. 6. Small variations in the initial drop volume also affect the ring's radius. Second, the supracluster size strongly depends on $h_0$, with bigger supraclusters obtained on thicker films, see Fig. 4b. In part, this is caused by an increase of the supracluster width $w$, which shows a linear correlation with $h_0$, as shown in Fig. 7.

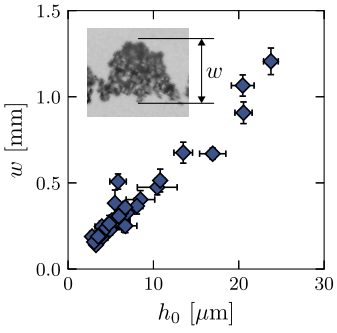


**Fig. 7.** Final width of the supraclusters ($w$, defined in the inset) as a function of the film thickness ($h_0$) with $c_d = 10$ wt% and $c_f = 30$ wt%. The width is determined for each supracluster in the ring. Each data point is the average of those values, with the vertical errorbar indicating the standard deviation. The horizontal errorbar indicates the standard deviation of five thickness measurements at five different locations on the film.

## 4. Dynamics and correlation with cluster formation

Based on Fig. 1 we identify a separation of time scales—the initial spreading dynamics are $\mathcal{O}(10^{-2}$ s), whereas the outward motion of the ring is $\mathcal{O}(1$ s). As we explain below, these two time scales correspond to two distinct spreading mechanisms: inertial drop spreading and Marangoni spreading. We demonstrate that the formation of the ring correlates with the Marangoni spreading, and we propose a kinematic model for the shape of the supraclusters.

### 4.1. Spreading dynamics

#### 4.1.1. Inertial spreading

When the drop first makes contact with the saline water film it spreads rapidly until it reaches an equilibrium shape determined by surface energies. This problem has been previously studied for the case of pure fluids, i.e., without any colloidal particles. For low-viscosity pure liquids, the inertial spreading dynamics of a drop are dictated by a balance between capillarity and inertia, such that

$$\frac{r_b}{R} \propto \left(\frac{t}{\tau}\right)^{\frac{1}{2}}, \quad \text{with} \quad \tau = \left(\frac{\rho R^3}{\gamma}\right)^{\frac{1}{2}}, \tag{1}$$

where $r_b$ is the base radius of the spreading drop, $R$ is the initial radius of the drop before contact, $t$ is the time, $\tau$ is the inertio-capillary time scale, $\rho$ is the density of the drop, and $\gamma$ is the surface tension of the drop [31,32]. The dynamics arises from the transformation of capillary energy into the kinetic energy of the liquid inside the moving meniscus. Equation (1) was found to be independent of the substrate properties and is valid for drops spreading on liquid substrates [33,34]. The drop is not engulfed by liquid from the saline water film since the surface tension of the film is higher than that of the drop. As such, the surface tension $\gamma$ in Eq. (1) is that of the drop [34–36]. Fig. 8a shows the base radius (measured from the side view perspective) as a function of time, scaled according to Eq. (1). The solid black line in Fig. 8a is Eq. (1) with

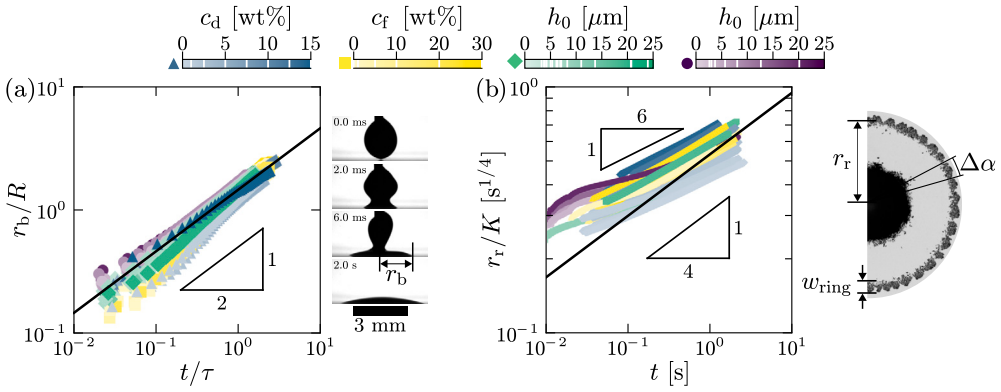


**Fig. 8.** Two types of spreading dynamics. For all experiments the reference system was $c_d = 10$ wt%, $c_f = 30$ wt%, and $h_0 \approx 10$ µm, with one of the parameters being varied in each of the experiment series; the value of that parameter is indicated by the white lines in the colour bars (45 experiments are shown in total; the legend applies to both panels). For the series indicated by purple circles $c_d = 0$ in addition to $h_0$ being varied. (a) Scaled base radius of the drop $r_b$ versus scaled time $t$. The solid black line is Eq. (1) with pre-factor 1.46. (b) Scaled ring radius $r_r$ versus time $t$. The solid black line is Eq. (2) with pre-factor 0.54. For the experiments with $c_d = 0$ we define $r_r$ as the inside radius of the Marangoni rim. (For interpretation of the colours in the figure(s), the reader is referred to the web version of this article.)

fitted pre-factor 1.46—a similar pre-factor was found for drop spreading on liquid substrates without colloidal particles in the drop [34].

Surprisingly, we find that the presence of colloidal particles in the drop and their destabilisation by the cations in the liquid substrate have no significant effect on the spreading dynamics. We are not aware of any previous studies of spreading of colloidal drops on thin saline water films. This indicates that particle destabilisation is limited to a small region close to the substrate surface, and that most of the colloidal particles in the bulk of the drop have not yet clustered when the drop is (inertially) spreading. This statement is further supported by the following scaling argument. In the absence of significant flow-induced mixing of the two liquids (the Reynolds number $\mathrm{Re} = \rho(\mathrm{d}r_b/\mathrm{d}t)h_0/\eta = \mathcal{O}(1)$) diffusion governs the motion of cations into the drop [16]. The diffusion length scale is $L \approx (Dt)^{1/2}$ [37], whereas the length scale associated with inertial spreading is $r_b \approx R(t/\tau)^{1/2}$, such that $L/r_b \approx (D\tau)^{1/2}/R$. The typical values associated with diffusion and inertial spreading in our experiments are $D = \mathcal{O}(10^{-9}$ m$^2$/s), $\tau = \mathcal{O}(10^{-3}$ s), and $R = \mathcal{O}(10^{-3}$ m). We thus find that $L/r_b = \mathcal{O}(10^{-3})$, indicating that the role of diffusion during the initial inertial spreading dynamics is negligible. The clustering of particles is therefore limited to the regions of direct contact between the colloidal suspension and the thin saline water film. The radius of the rings grows even after the centre drop has stopped spreading. This suggests that inertial drop spreading is not the only spreading mechanism involved in the pattern formation process.

#### 4.1.2. Marangoni spreading

A key ingredient that is not accounted for in the description of inertial spreading is that the surface tensions of the colloidal suspension and the $CaCl_2$ solution are different (see Fig. S3 in Sec. S3 of the Supplementary Material). When the low surface tension colloidal drop comes into contact with the high surface tension saline water film, a strong surface tension gradient emerges, which results in a Marangoni-driven flow known as 'Marangoni spreading' [11]. Adapting the method of Hernández-Sánchez et al., who considered Marangoni spreading due to a stream of alcohol on a film of pure water, we can derive a scaling law for the expected time evolution of the radius of the ring $r_r$ [11]. The flow inside the saline film is driven by the Marangoni stress ($\propto \Delta\gamma/r_r$) and opposed by the viscous stress ($\propto \eta(\mathrm{d}r_r/\mathrm{d}t)/h$). Here, $h$ is the characteristic thickness of the circular thin region in the film that remains on the substrate for radii smaller than $r_r$ (see Fig. 2), which can be determined using volume conservation. The volume of the thin region is approximately equal to the initial volume of the drop such that $\pi r_r^2 h \sim V$ [11]. By balancing the stresses we then find

$$r_r \propto K t^{\frac{1}{4}}, \quad \text{with} \quad K = \left(\frac{V\Delta\gamma}{\eta}\right)^{\frac{1}{4}}, \tag{2}$$

where $r_r$ is the radius of the ring, $V$ is the volume of the drop, and $\eta$ is the viscosity of the saline water film. In Fig. 8b we show the ring radius as a function of time, scaled according to Eq. (2). The solid black line in Fig. 8b is Eq. (2) with fitted pre-factor 0.54. While Eq. (2) correctly predicts the order of magnitude of $r_r$, the experimental data does not precisely match the predicted exponent 1/4. Rather, we find that an exponent of approximately 1/6 best matches the experimental data. This discrepancy may be caused by the initial inertial spreading dynamics (and subsequent crossover into Marangoni spreading dynamics) and the finite size of the drop ($r_r/R \gg 1$ in Hernández-Sánchez et al. [11], whereas here $r_r/R \sim 1$); the effects of both are not included in Eq. (2). However, the scaling law in Eq. (2) provides the correct order of magnitude over two orders of time. Furthermore, we note that the quantitative mismatch between Eq. (2) and the measured spreading dynamics is not critical to the interpretations put forward in Secs. 4.2 and 4.3; both are based on the measured film properties and spreading dynamics, and neither uses Eq. (2) explicitly.

### 4.2. Mechanism of ring formation

Marangoni spreading involves the appearance of a rim, which can indeed be directly correlated to the formation of the ring-shaped pattern. Marangoni flows induced by surfactants [38–41] or mixtures [11] have been known to lead to the opening of a circular thin region in the film, surrounded by a 'rim' that collects the volume displaced from the thin region—reminiscent of the classical dewetting problem [42]. We indeed observe the formation of such a 'Marangoni rim' in our system (see Fig. 2, for a case without any colloidal particles in the drop).

The shape of the rim and its direct correlation with the clusters is revealed in Fig. 9, which reports typical DHM measurements. Fig. 9a shows the location of the supracluster with respect to the Marangoni rim from a top view perspective. In Fig. 9b we show a cross section that shows that the supracluster is located slightly in front of the Marangoni rim's maximum on the outward flank of the rim. In Fig. 9c we track the location of the maximum of the Maragoni rim and the centre of mass of the supracluster over time and show that the supracluster moves faster than the Marangoni rim (see Fig. S10 in Sec. S8 of the Supplementary Material). This difference in velocity is evidence for the ability of the Marangoni-induced stress gradient to transport (supra)clusters, which is essential for the formation of the ring-shaped pattern.

Another feature readily explained by the Marangoni rim's role in the pattern formation process is the $h_0$ dependence shown in Figs. 4

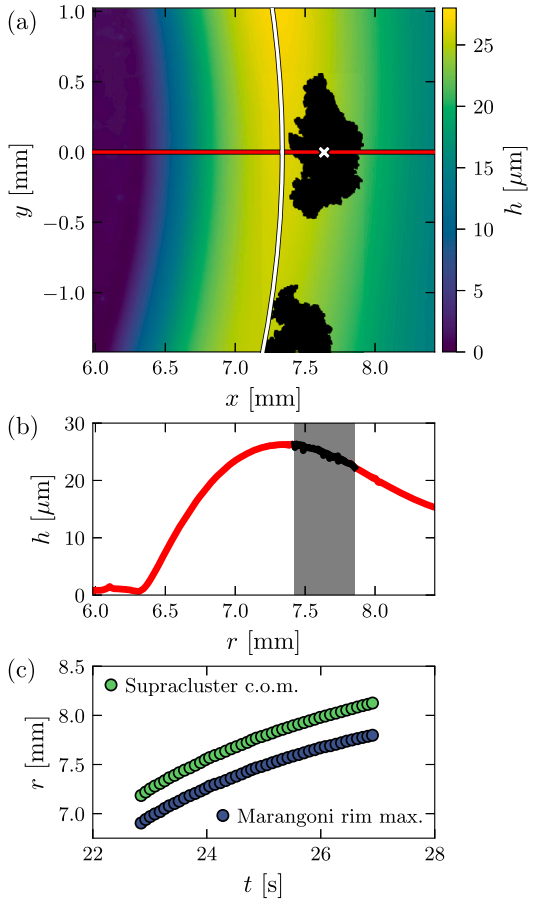


**Fig. 9.** DHM measurement of the location of a supracluster with respect to morphological properties of the Marangoni rim ($t = 5.6$ s, $h_0 \approx 13$ μm, $c_d = 10$ wt%, $c_f = 30$ wt%). (a) Morphology $h(x, y)$ of a region of the Marangoni rim with superclusters (black areas). The white line is a circle fitted through the radial maxima of the Marangoni rim ($y$-coordinates with clusters were excluded from the fitting procedure). The white cross indicates the centre of mass of the supracluster that is fully in the field of view. The origin of the coordinate system is the location where the colloidal drop was deposited. (b) Surface profile of a Marangoni rim with a cluster, extracted along the red line in panel (a). The grey zone indicates the location of a supracluster (the DHM measurement is noisy in this zone, and thus the surface profile cannot be accurately measured; see Fig. S2 in Sec. S2 of the Supplementary Material). (c) The centre of mass of the supracluster is consistently ahead of the Marangoni rim's maximum; both move at approximately the same velocity.

and 7. The volume of the displaced liquid increases with $h_0$, and so does the width of the Marangoni rim. This is confirmed in Fig. S11 in Sec. S9 of the Supplementary Material, where we show the Marangoni rim in the absence of colloidal particles (i.e., with $c_d = 0$) for several $h_0$. The amount of particle clusters is set by the width of the rim, see Fig. S12 in Sec. S10 of the Supplementary Material. The supracluster size and width—limited by the amount of particle clusters on the rim after it separates from the drop—are thus determined by the width of the Marangoni rim and therefore depend on $h_0$.

### 4.3. Trapezoidal supracluster shape: a kinematic explanation

Why are the superclusters mostly trapezoidally shaped (see the inset of Fig. 1)? We demonstrate a correlation between the shapes of the superclusters and the radial growth dynamics—inertial spreading followed by Marangoni spreading—suggesting a purely kinematic origin of the trapezoids.

In Fig. 10a we show the time evolution of the contact line and superclusters as a function of the azimuthal coordinate $\alpha$ for a typical pattern. All prominent features (i.e., undulations of the contact line and supracluster locations) remain at a constant $\alpha$ over time, demonstrating that the motion of the colloidal liquid and (supra)clusters is purely radial. Hence, all particle clusters that join the inner edge of the ring are distributed over an arc with length $l(t) \approx r(t)\Delta\alpha$, with $\Delta\alpha$ as indicated in Fig. 8b. Initially, $r(t)$ is close to the inertial spreading of the base radius $r_b(t)$, while it later follows the Marangoni rim dynamics $r_r(t)$. Patching the two regimes together, we find $r(t)$ as indicated in Fig. 10b, where $t$ is the time at which the particles join the ring. Our proposition for the trapezoidal supracluster shape (marked as $\hat{y}$ vs $\hat{x}$ in Fig. 10c) is based on the remarkable similarity with the radial growth dynamics shown (marked as $t$ vs $r$ in Fig. 10b; the axes are rotated from their conventional orientation to highlight the similarity). This suggests that the width of the clusters is set by the radial width dynamics $\hat{x}(t) \approx r(t)\Delta\alpha$, with the temporal history encoded in $\hat{y}(t)$.

To test this kinematic hypothesis, we need to complement the dynamics $\hat{x}(t) \approx r(t)\Delta\alpha$ with an estimate for $\hat{y}(t)$; this will offer a prediction for the supracluster shape that can be directly compared to the experimental measurement. We assume that the width grows linearly in time, $\hat{y}(t) = vt$, where $v$ is a growth rate. We estimate this velocity as $v \approx w/t_{sep}$, where the final width $w$ is defined in Fig. 7, while $t_{sep}$ is the time at which the superclusters separate from each other. For the example shown in Fig. 10c, $w \approx 355$ μm and $t_{sep} \approx 0.48$ s (see Movie S2 in the Supplementary Material). From Fig. 10a we find that $\Delta\alpha \approx 0.17$ rad, obtained by averaging all $\Delta\alpha$ between the vertical dotted lines. The red line in Fig. 10c shows $\hat{y}(t)$ versus $\hat{x}(t)$ according to the prediction of the kinematic model. We find reasonable agreement between the measured supracluster shape and the shape as predicted by the model. The trapezoidal supracluster shape can thus be understood from the two types of dynamics—the flat top of the supracluster corresponds to the rapid inertial spreading dynamics, while its slanting sides correspond to the slower Marangoni spreading dynamics.

## 5. Conclusion and outlook

We have revealed a novel pattern formation mechanism—ring-shaped patterns of colloidal superclusters appear when a colloidal drop is deposited on a thin saline water film. A delicate balance between the fluid-mechanical and physicochemical properties of the system governs the pattern. We show that the trapezoidal shape of the superclusters is determined by the transition from inertial spreading dynamics to Marangoni spreading.

As a future perspective, a next step from the fluid-mechanical perspective could be to investigate the effect of different dynamics on the supracluster shape. This could be achieved by using a more viscous colloidal drop, such that the initial inertial spreading phase is of viscous nature instead. Viscous spreading implies a much larger typical time-scale and different dynamics with $r_{b,viscous}(t) \propto t$ instead of $r_{b,inertial}(t) \propto t^{1/2}$. According to the proposed model this would affect the shape of the superclusters. We hope that our results motivate the realisation of modelling approaches that account for the intricate hydrodynamic interactions coupled to the destabilisation of the colloidal drop. The experiments provide detailed benchmarks for such future developments. From the physicochemical perspective, it would be interesting to investigate different particle sizes and shapes, and different combinations of particle types and salts. For example, it has been shown that using $MgCl_2$ instead of $CaCl_2$ results in denser particle clusters [16]. The destabilisation of colloidal particles is also affected by the valency of the cations, with a lower concentration of cations being required to induce particle destabilisation with increasing valency (the Schulze-Hardy rule). Hence, it would be interesting to investigate the systems' behaviour with monovalent and trivalent salts such as NaCl or $AlCl_3$ [5,43].

In inkjet printing, solidification of ink is typically achieved by letting the ink drops evaporate on the substrate [4]. It is difficult to achieve uniform particle deposits using this method due to the so-called

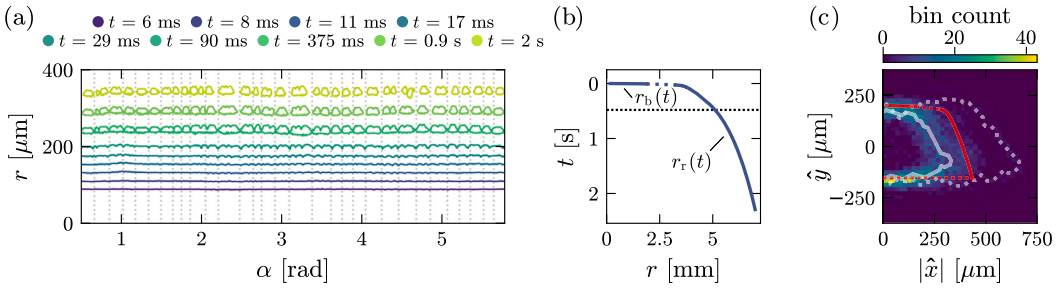


**Fig. 10.** (a) Time evolution of the contact line and supraclusters with respect to the centre of the pattern for $c_d = 2.5$ wt%, $c_f = 30$ wt%, and $h_0 \approx 9$ μm (same data as in Fig. 3c). The shadow of the syringe complicates the image analysis; for this reason we show only the interval $\alpha \in [1/2, 2\pi - 1/2]$ rad. The dotted lines are guides to the eye with constant $\alpha$ at prominent features. (b) The spreading radius as a function of time. This radius is given by the base radius $r_b(t)$ initially, and at later times by the ring radius $r_r(t)$. The dotted line connects the two spreading regimes; the ring separates from the centre drop in this transitional regime, such that it is difficult to accurately define the spreading radius. The black dotted line indicates the time at which the final clusters join the ring, and is the (approximate) time at which the supraclusters reach their final shape (cf., panel (a)). (c) Two-dimensional histogram of the final supracluster shapes of the same experiment as shown in (a); based on 92 supracluster halves. The centre of each supracluster is located at $(\hat{x}, \hat{y}) = (0, 0)$, and each supraclusters is rotated by the angle $\alpha$ in panel (a). The resolution of the camera (19.7 μm/pixel) was used to set the bin width in both directions. An example outline of a supracluster (solid white line) and an example outline of two supraclusters that did not fully separate (dashed white line) are also shown. The red line shows the calculated supracluster shape, the line style (solid, dotted) corresponds to that of panel (b). We have shifted the calculated shape aslong the $\hat{y}$-direction such that the centre of the calculated shape is located at $(\hat{x}, \hat{y}) = (0, 0)$. See the Supplementary Material for the corresponding movie (Movie S2) and a similar analysis of another pattern (Fig. S13 in Sec. S11).

'coffee-stain effect', as well as other phenomena such as phase segregation, crystallisation, and the influence of neighbouring drops [44–47]. Extensive research has been devoted to achieving uniform particle deposits by modifying the liquid properties of the drop, for example by the inclusion of surfactants or polymers [48,27]. Our results show that salt-induced solidification, such as used in wet-on-wet printing [6,19], is a viable alternative to evaporation-driven solidification: the properties of the salt-containing primer layer can be tailored (using Figs. 5 and 6 as guidance) such that the supracluster ring does not appear and a uniform particle deposit is achieved (as in Fig. 5a-c). Contrary to the aforementioned strategies employed to achieve uniform particle deposits in evaporation-driven solidification, this method does not need modification of the ink (as long as its pigment is electrostatically stabilised). Moreover, we expect the influence of neighbouring drops to be limited as the particle deposition occurs on a shorter timescale than the effects of evaporation or capillary interactions [6]. Other applications, such as those related to micro-patterning, may instead want to promote the formation of the supracluster ring as a way to generate particle clusters of a certain shape and size. Our results show that a wide range of supracluster sizes can be achieved by tuning $c_d$, $c_f$, and $h_0$.

## CRediT authorship contribution statement

**Michiel A. Hack:** Writing – review & editing, Writing – original draft, Visualization, Validation, Software, Methodology, Investigation, Formal analysis, Data curation, Conceptualization. **Marjolein N. van der Linden:** Writing – review & editing, Validation, Supervision, Resources, Project administration, Investigation. **Herman Wijshoff:** Writing – review & editing, Validation, Supervision, Resources, Project administration, Methodology, Investigation, Funding acquisition, Formal analysis, Conceptualization. **Jacco H. Snoeijer:** Writing – review & editing, Writing – original draft, Visualization, Validation, Supervision, Software, Resources, Project administration, Methodology, Investigation, Funding acquisition, Formal analysis, Data curation, Conceptualization. **Tim Segers:** Writing – review & editing, Writing – original draft, Visualization, Validation, Supervision, Software, Resources, Project administration, Methodology, Investigation, Formal analysis, Data curation, Conceptualization.

## Declaration of competing interest

The authors declare that they have no known competing financial interests or personal relationships that could have appeared to influence the work reported in this paper.

## Data availability

Data will be made available on request.

## Acknowledgements

We thank Detlef Lohse for stimulating discussions. This work is part of an Industrial Partnership Programme (IPP) of the Netherlands Organization for Scientific Research (NWO). This research programme is cofinanced by Canon Production Printing Netherlands B.V., University of Twente and Eindhoven University of Technology. We also acknowledge support from Detlef Lohse's ERC Advanced Grant No. 740479/DDD/ERC-2016-ADG out of which the DHM facility was financed.

## Appendix A. Supplementary material

Supplementary material related to this article can be found online at https://doi.org/10.1016/j.jcis.2024.06.015.

## References

[1] K.G. Winkels, I.R. Peters, F. Evangelista, M. Riepen, A. Daerr, L. Limat, J.H. Snoeijer, Receding contact lines: from sliding drops to immersion lithography, Eur. Phys. J. Spec. Top. 192 (2011) 195–205, https://doi.org/10.1140/epjst/e2011-01374-6.
[2] H. Wijshoff, The dynamics of the piezo inkjet printhead operation, Phys. Rep. 491 (2010) 77–177, https://doi.org/10.1016/j.physrep.2010.03.003.
[3] H. Wijshoff, Drop dynamics in the inkjet printing process, Curr. Opin. Colloid Interface Sci. 36 (2018) 20–27, https://doi.org/10.1016/j.cocis.2017.11.004.
[4] D. Lohse, Fundamental fluid dynamics challenges in inkjet printing, Annu. Rev. Fluid Mech. 54 (2022) 349–382, https://doi.org/10.1146/annurev-fluid-022321-114001.
[5] M.A. Mulla, H.N. Yow, H. Zhang, O.J. Cayre, S. Biggs, Colloid particles in ink formulations, in: S.D. Hoath (Ed.), Fundamentals of Inkjet Printing: The Science of Inkjet and Droplets, Wiley-VCH, Weinheim, Germany, 2016, pp. 141–168.
[6] M.A. Hack, M. Costalonga, T. Segers, S. Karpitschka, H. Wijshoff, J.H. Snoeijer, Printing wet-on-wet: attraction and repulsion of drops on a viscous film, Appl. Phys. Lett. 113 (2018) 183701, https://doi.org/10.1063/1.5048681.
[7] D. Bonn, J. Eggers, J. Indeku, J. Meunier, E. Rolley, Wetting and spreading, Rev. Mod. Phys. 81 (2009) 739–805, https://doi.org/10.1103/RevModPhys.81.739.
[8] D. Lohse, X. Zhang, Physicochemical hydrodynamics of droplets out of equilibrium, Nat. Rev. Phys. 2 (2020) 426–443, https://doi.org/10.1038/s42254-020-0199-z.
[9] S. Karpitschka, F. Liebig, H. Riegler, Marangoni contraction of evaporating sessile droplets of binary mixtures, Langmuir 33 (2017) 4682–4687, https://doi.org/10.1021/acs.langmuir.7b00740.
[10] M.A. Hack, W. Kwieciński, O. Ramírez-Soto, T. Segers, S. Karpitschka, E.S. Kooij, J.H. Snoeijer, Wetting of two-component drops: Marangoni contraction versus autophobing, Langmuir 37 (2021) 3605–3611, https://doi.org/10.1021/acs.langmuir.0c03571.

[11] J.F. Hernández-Sánchez, A. Eddi, J.H. Snoeijer, Marangoni spreading due to a localized alcohol supply on a thin water film, Phys. Fluids 27 (2015) 032003, https://doi.org/10.1063/1.4915283.
[12] M. Motaghian, R. Shirsavar, M. Erfanifam, M. Sabouhi, E. van der Linden, H.A. Stone, D. Bonn, M. Habibi, Rapid spreading of a droplet on a thin soap film, Langmuir 35 (2019) 14855–14860, https://doi.org/10.1021/acs.langmuir.9b02274.
[13] D.K. Sinz, M. Hanyak, A.A. Darhuber, Immiscible surfactant droplets on thin liquid films: spreading dynamics, subphase expulsion and oscillatory instabilities, J. Colloid Interface Sci. 364 (2011) 519–529, https://doi.org/10.1016/j.jcis.2011.08.055.
[14] L. Keiser, H. Bense, P. Colinet, J. Bico, E. Reyssat, Marangoni bursting: evaporation-induced emulsification of binary mixtures on a liquid layer, Phys. Rev. Lett. 118 (2017) 074504, https://doi.org/10.1103/PhysRevLett.118.074504.
[15] L. Keiser, H. Bense, P. Colinet, J. Bico, E. Reyssat, Marangoni-driven flower-like patterning of an evaporating drop spreading on a liquid substrate, Nat. Commun. 9 (2018) 820, https://doi.org/10.1038/s41467-018-03201-3.
[16] A. Oko, A. Swerin, B.D. Brandner, D. Bugner, W. Cook, P.M. Claesson, Aggregation of inkjet ink components by Ca and Mg ions in relation to colorant pigment distribution paper, Colloids Surf. A 456 (2014) 92–99, https://doi.org/10.1016/j.colsurfa.2014.05.023.
[17] G. Venditti, V. Murali, A.A. Darhuber, Chromatographic effects in inkjet printing, Langmuir 37 (2021) 11726–11736, https://doi.org/10.1021/acs.langmuir.1c01624.
[18] A. Fraters, M. van den Berg, Y. de Loore, H. Reinten, H. Wijshoff, D. Lohse, M. Versluis, T. Segers, Inkjet nozzle failure by heterogeneous nucleation: bubble entrainment, cavitation, and diffusive growth, Phys. Rev. Appl. 12 (2019) 064019, https://doi.org/10.1103/PhysRevApplied.12.064019.
[19] H. Hamada, D.W. Bousfield, Effect of cationic additives on ink penetration, J. Pulp Pap. Sci. 35 (2009) 118–122.
[20] I. Szilagyi, A. Sadeghpour, M. Borkovec, Destabilization of colloidal suspensions by multivalent ions and polyelectrolytes: from screening to overcharging, Langmuir 28 (2012) 6211–6215, https://doi.org/10.1021/la300542y.
[21] E.J.W. Verwey, J.T.G. Overbeek, Theory of the Stability of Lyophobic Colloids, Elsevier Publishing Company, Amsterdam, 1948.
[22] M.K. Kim, Principles and techniques of digital holographic microscopy, SPIE Rev. 1 (2010) 018005, https://doi.org/10.1117/6.0000006.
[23] Y. Emery, T. Colomb, E. Cuche, Metrology applications using off-axis digital holography, J. Phys. Photon. 3 (2021) 034016, https://doi.org/10.1088/2515-7647/ac0957.
[24] T. Liu, R. J. Nick, Modified pigment containing inkjet ink compositions having a reduced conductivity increase, U.S. Patent 8,147,604 B2, 2012.
[25] D. Okamura, K. Yamasaki, K. Moribe, K. Okumura, K. Shiiba, H. Kishi, Ink jet ink, ink cartridge, and ink jet recording method, U.S. Patent 9,243,155 B2, 2016.
[26] H. Hu, R.G. Larson, Evaporation of a sessile droplet on a substrate, J. Phys. Chem. B 106 (2002) 1334–1344, https://doi.org/10.1021/jp0118322.
[27] Y. Li, C. Diddens, T. Segers, H. Wijshoff, M. Versluis, D. Lohse, Evaporating droplets on oil-wetted surfaces: suppression of the coffee-stain effect, Proc. Natl. Acad. Sci. USA 117 (2020) 16756–16763, https://doi.org/10.1073/pnas.2006153117.
[28] C.-Y. Tan, Y.-X. Huang, Dependence of refractive index on concentration and temperature in electrolyte solution, polar solution, nonpolar solution, and protein solution, J. Chem. Eng. Data 60 (2015) 2827–2833, https://doi.org/10.1021/acs.jced.5b00018.
[29] H.-L. Zhang, G.-H. Chen, S.-J. Han, Viscosity and density of $H_2O$ + NaCl + $CaCl_2$ and $H_2O$ + KCl + $CaCl_2$ at 298.15 K, J. Chem. Eng. Data 42 (1997) 526–530, https://doi.org/10.1021/je9602733.
[30] P.G. Saffman, G.I. Taylor, The penetration of a fluid into a porous medium or Hele-Shaw cell containing a more viscous liquid, Proc. R. Soc. Lond. A 245 (1958) 312–329, https://doi.org/10.1098/rspa.1958.0085.
[31] A.-L. Biance, C. Clanet, D. Quéré, First steps in the spreading of a liquid droplet, Phys. Rev. E 69 (2004) 016301, https://doi.org/10.1103/PhysRevE.69.016301.
[32] K.G. Winkels, J.H. Weijs, A. Eddi, J.H. Snoeijer, Initial spreading of low-viscosity drops on partially wetting surfaces, Phys. Rev. E 85 (2012) 055301, https://doi.org/10.1103/PhysRevE.85.055301.
[33] B.B.J. Stapelbroek, H.P. Jansen, E.S. Kooij, J.H. Snoeijer, A. Eddi, Universal spreading of water drops on complex surfaces, Soft Matter 10 (2014) 2641–2648, https://doi.org/10.1039/c3sm52464g.
[34] A. Carlson, P. Kim, G. Amberg, H.A. Stone, Short and long time drop dynamics on lubricated substates, Europhys. Lett. 104 (3) (2013) 34008, https://doi.org/10.1209/0295-5075/104/34008.
[35] J.D. Smith, R. Dhiman, S. Anand, E. Reza-Garduno, R.E. Cohen, G.H. McKinley, K.K. Varanasi, Droplet mobility on lubricant-impregnated surfaces, Soft Matter 9 (2013) 1772–1780, https://doi.org/10.1039/C2SM27032C.
[36] F. Schellenberger, J. Xie, N. Encinas, A. Hardy, M. Klapper, P. Papadopoulos, H.-J. Butt, D. Vollmer, Direct observation of drops on slippery lubricant-infused surfaces, Soft Matter 11 (38) (2015) 7617–7626, https://doi.org/10.1039/c5sm01809a.
[37] P.-G. de Gennes, F. Brochard-Wyart, D. Quéré, Capillarity and Wetting Phenomena: Drops, Bubbles, Pearls, Waves, Springer, New York, 2004.
[38] D.P. Gaver, J.B. Grotberg, The dynamics of a localized surfactant on a thin film, J. Fluid Mech. 213 (1990) 127–148, https://doi.org/10.1017/S0022112090002257.
[39] M.R.E. Warner, R.V. Craster, O.K. Matar, Fingering phenomena created by a soluble surfactant deposition on a thin liquid film, Phys. Fluids 16 (2004) 2933–2951, https://doi.org/10.1063/1.1763408.
[40] A. Hamraoui, M. Cachile, C. Poulard, A.M. Cazabat, Fingering phenomena during spreading of surfactant solutions, Colloids Surf. A 250 (2004) 215–221, https://doi.org/10.1016/j.colsurfa.2003.12.035.
[41] X. Wang, E. Bonaccurso, J. Venzmer, S. Garoff, Deposition of drops containing surfactants on liquid pools: movement of the contact line, Marangoni ridge, capillary waves and interfacial particles, Colloids Surf. A 486 (2015) 53–59, https://doi.org/10.1016/j.colsurfa.2015.09.029.
[42] P.G. de Gennes, Solvent evaporation of spin cast films: “crust” effects, Eur. Phys. J. E 7 (2002) 31–34, https://doi.org/10.1140/epje/i200101169.
[43] L.H.N. Nukui, L.R.S. Barbosa, D.F.S. Petri, Impact of monovalent and divalent cations on the colloidal stability of negatively charged latex particles decorated with poly(ethyleneglycol), Ind. Eng. Chem. Res. 66 (2016) 606–614, https://doi.org/10.1021/acs.iecr.5b04103.
[44] R.D. Deegan, O. Bakajin, T.F. Dupont, G. Huber, S.R. Nagel, T.A. Witten, Capillary flows as the cause of ring stains from dried liquid drops, Nature 389 (1997) 827–829, https://doi.org/10.1038/39827.
[45] H. Tan, C. Diddens, P. Lv, J.G.M. Kuerten, X. Zhang, D. Lohse, Evaporation-triggered microdroplet nucleation and the four life phases of an evaporating ouzo drop, Proc. Natl. Acad. Sci. USA 113 (2016) 8642–8647, https://doi.org/10.1073/pnas.1602260113.
[46] Y. Li, V. Salvator, H. Wijshoff, M. Versluis, D. Lohse, Evaporation-induced crystallization of surfactants in sessile multicomponent droplets, Langmuir 36 (2020) 7545–7552, https://doi.org/10.1021/acs.langmuir.0c01169.
[47] N.J. Cira, A. Benusiglio, M. Prakash, Vapour-mediated sensing and motility in two-component droplets, Nature 519 (2015) 446–450, https://doi.org/10.1038/nature14272.
[48] H. Kim, F. Boulogne, E. Um, I. Jacobi, E. Button, H.A. Stone, Controlled uniform coating from the interplay of Marangoni flows and surface-adsorbed macromolecules, Phys. Rev. Lett. 116 (2016) 124501, https://doi.org/10.1103/PhysRevLett.116.124501.